CRYSTAL GROWTH & DESIGN

Article

pubs.acs.org/crystal

Step-Flow Growth of Bi_2Te_3 Nanobelts

Piet Schönherr,[†] Thomas Tilbury,[†] Haobei Wang,[†,§] Amir A. Haghighirad,[†] Vesna Srot,[‡] Peter A. van Aken,[‡] and Thorsten Hesjedal*[,†]

[†]Clarendon Laboratory, Department of Physics, University of Oxford, Oxford, England

[‡]Stuttgart Center for Electron Microscopy (StEM), Max Planck Institute for Solid State Research, Stuttgart, Germany

[§]University of Science and Technology of China, Hefei, Anhui, China

ABSTRACT: Understanding the growth mechanism of nanostructures is key to tailoring their properties. Many compounds form nanowires following the vapor−liquid−solid (VLS) growth mechanism, and the growth of Bi_2Te_3 nanobelts was also explained following the VLS route. Here, we present another growth mechanism of Bi_2Te_3 nano- and submicron belts and ribbons. The samples were grown by physical vapor transport from Bi_2Te_3 precursors using TiO_2 nanoparticles as a catalyst and analyzed by scanning electron microscopy and scanning transmission electron microscopy. The growth starts from a Te-rich cluster and proceeds via a thin, tip-catalyzed primary layer growing in the [110] direction. The primary layer serves as a support for subsequent step-flow growth. The precursor predominantly absorbs on the substrate and reaches the belt by migration from the base to the tip. Terrace edges pose energy barriers that enhance the growth rate of secondary layers compared to the primary layer. Broadening of the sidewalls is commonly observed and leads to triangular voids that can even result in a branching of the growing belts. Step-flow growth of Bi_2Te_3 submicron belts is different from the spiral-like growth mode of Bi_2Te_3 thin films and an important step toward the growth of layered topological insulator nanostructures.

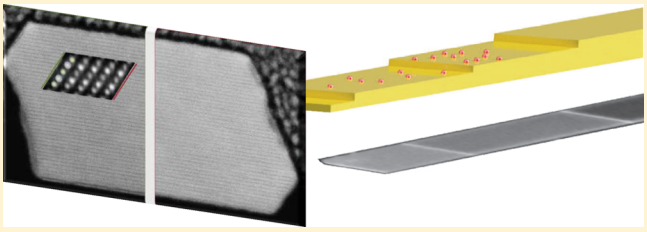

INTRODUCTION

Belt-like nanostructures typically show a rectangular cross-section with a height on the nanoscale and a width from hundreds of nanometers to several micrometers. Nanobelts (or nanoribbons) of semiconductors and metal oxides were intensely studied over the past two decades with electronic and sensor applications in mind.[1−7] For instance, SnO_2 nanobelts grow in a self-catalyzed process and are sensitive building blocks for NO_2 gas sensors.[8] Materials with a layered crystal structure such as the chalcogenides Sb_2Te_3, Bi_2Se_3, and Bi_2Te_3 are ideal candidates for nanobelt growth since they preferentially grow parallel to the layers.[7] Bi_2Te_3 is a thermoelectric material with a high figure of merit, as well as a topological insulator (TI), which is a new state of quantum matter.[9,10] The promise of TIs for device applications has led to a surge of interest in Bi_2Te_3 nanomaterials due to inherent (relative) suppression of unwanted bulk carriers.[11−13] Bi_2Te_3 has a rhombohedral crystal structure with space group D^5_{3d} ($R\bar{3}m$). The unit cell of Bi_2Te_3 is a stack of three ∼1 nm-high quintuple layers (QLs) formed by the $Te^{(1)}$−Bi−$Te^{(2)}$−Bi−$Te^{(1)}$ atomic layer sequence, perpendicular to the *c*-axis. The QLs are separated by a van-der-Waals gap, which makes Bi_2Te_3 highly anisotropic with strong in-plane interatomic bonds and weak bonds between two QLs. Hence, adatoms prefer to attach to the *c*-plane to minimize their free energy in growth experiments. Chalcogenide nanobelts have been employed as building blocks for flexible and transparent electrode applications, hybrid Dirac materials, and photodetectors;[14−16] however, little attention has been paid to a thorough understanding of the growth mechanism.[17]

For thin film growth, one would intuitively assume that the preferential saturation of the stronger in-plane bonds results in a smooth, layer-by-layer step-flow growth. In contrast, however, film growth is dominated by a hillock growth mechanism that leads to alternating edge dislocation pairs, twin boundaries, and an effective roughening of the surface through spiral-like features that grow along the *c*-axis.[18−21] Nanowires and nanobelts, on the other hand, exhibit smooth surfaces and grow essentially single crystalline.[7] Recent advances in research on chalcogenide nanowires, nanoribbons, and submicron belts call for an in-depth analysis of the growth of these structures.[22,23] The common growth technique is catalyzed vapor transport. Atmospheric pressure (compared to low-vacuum vapor transport) and high carrier gas flow rates (100−300 sccm) are crucial for the growth of these Bi_2Te_3 structures.[24,25] Catalysts such as sputtered Au thin films,[7,26,27] colloidal Au nanoparticles with diameters between 5 and 20 nm,[28−30] or TiO_2 nanoparticles[25,31] can be employed to increase the yield and length of these structures.

Here, we discuss the growth mechanism of Bi_2Te_3 nano- and sub-micrometer-sized structures. Growth is initialized by nucleation on the TiO_2 particles, proceeding via the formation

Received: August 2, 2016
Revised: November 1, 2016
Published: November 1, 2016

DOI: 10.1021/acs.cgd.6b01147
Cryst. Growth Des. 2016, 16, 6961−6966

of the first QLs that grow away from the seeds, until finally the direct vapor−solid growth of further layers becomes possible. Here, we will refer to all belt- or ribbon-like structures, independent of size, as "belts" for simplicity. We highlight two examples of unique growth morphologies to pin down the epitaxial van-der-Merwe growth mode as a model for thin film growth. The results are equally applicable to Bi_2Se_3 and Sb_2Te_3 belts due to the similarity in the crystal structure and observations from similar growth experiments (not shown).

EXPERIMENTAL SECTION

The Bi_2Te_3 precursor (powder) was placed at the center of a 1″-diameter tube furnace (Nabertherm B180), fitted with a quartz tube. The furnace was kept at 585 °C, and the vapor was carried downstream by a laminar flow of N_2 at a rate of 150−300 sccm, as shown in Figure 1a. Because of precursor decomposition, the color of the deposit on the walls of the quartz tube changes from silver (Bi_2Te_3) to gray (Te) toward the colder end along the temperature profile. Clean Si(100) substrates were coated with the binding agent poly-L-lysine (PLL). A homemade TiO_2 nanoparticle solution made from a mixture of phases, P-25, was applied as catalyst in order to increase the yield similar to the procedure described previously.[25,31] Then the substrates were placed at a position in the furnace where the temperature is ∼480 °C. The furnace was ramped to growth temperature within 20 min, and the temperature was held constant for 60 min. Then the furnace was allowed to cool down naturally. As-grown samples were characterized by scanning electron microscopy (SEM). Samples in cross-sectional geometry were prepared by focused ion beam (FIB) for high-angle annular dark-field scanning transmission electron microscopy (HAADF-STEM) and energy-dispersive X-ray spectroscopy (EDX-STEM) at 200 kV on a JEOL ARM200F (JEOL Co. Ltd.), equipped with a cold field-emission gun and a DCOR probe Cs corrector (CEOS Co. Ltd.). EDX data were obtained using a 100 mm^2 JEOL Centurio SDD-EDX detector (JEOL Co. Ltd.) and the Thermo Noran System 7 EDX system (Thermo Fisher Scientific Inc.). The TEM data were analyzed using Digital Micrograph (Gatan Inc.) and for HAADF-STEM image noise removal a multivariate statistical analysis plug-in (HREM Research Inc.) and a script function written by D.R.G. Mitchell were used.

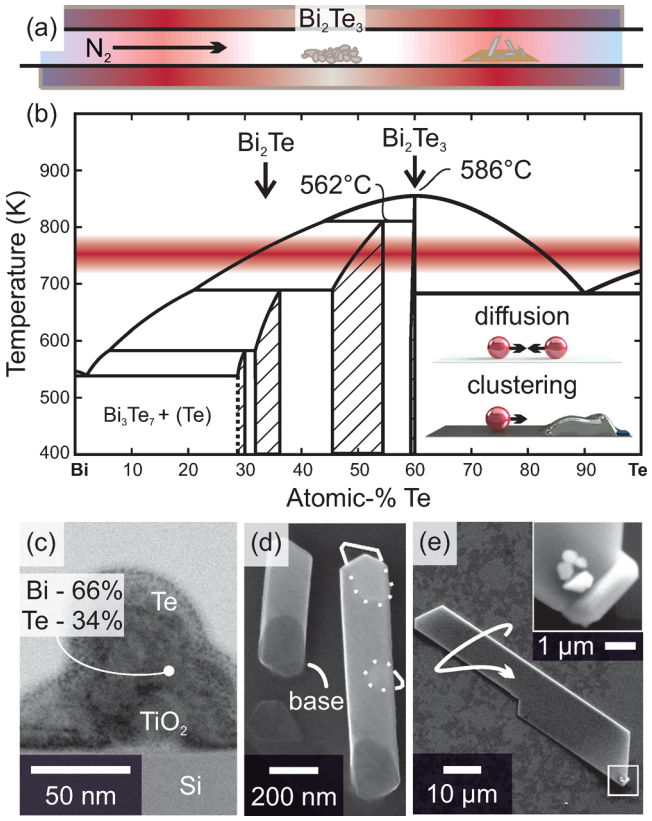

Figure 1. (a) Bi_2Te_3 is evaporated in the center of the furnace and decomposes before reaching the substrate placed downstream at its cold end. (b) Simplified Bi−Te phase diagram.[32] The growth temperature is marked by a red bar. The inset shows diffusion of atoms and molecules (red spheres) toward TiO_2 nanoparticles. (c) These clusters incorporate TiO_2 catalyst particles (brighter circular areas), as can be seen in the STEM image. Their composition is Bi_2Te (darker region), surrounded by an outer Te shell (brighter region). The composition is given in atomic-%, as measured by EDX. (d) Free-standing belts (SEM micrograph) grown from a flat base (dark). The belts are transparent so that underlying plates (indicated by white outlines) are visible. (e) Image of the base of a belt showing several particles at its root (inset) which potentially act as an initial nucleation center. The belt has been rotated manually by 180° about its long axis (white arrow).

RESULTS AND DISCUSSION

Microscopic Picture of the Growth. The microscopic model of Bi_2Te_3 belt growth consists of four steps: (1) chemical decomposition of the precursor molecules (at higher temperature) and transport to the substrate, (2) cluster formation on the substrate, (3) nucleation, and (4) growth. Bi_2Te_3 vapor decomposes according to

$$2Bi_2Te_3 \rightarrow 4Bi + 3Te_2$$

when evaporated as described above. Bi atoms and Te_2 molecules that are adsorbed onto the Si substrate either desorb again or migrate over the surface within their diffusion length, forming clusters as shown in the inset to Figure 1b.

The stability of these clusters depends on temperature, cluster size, and binding energies. Bi_2Te_3 clusters are stable at a radius of about 10 nm at 300 °C, as known from thin film growth.[33] The substrate temperatures for belt growth are 30−40% higher, leading to a higher density of smaller clusters. These initial liquid nucleation centers must be formed by Te molecules since at the growth temperature, the Bi_2Te_3 phase is only accessible via a Te-rich melt, as can be seen in the binary phase diagram in Figure 1b. A Bi-rich melt, on the other hand, only forms Bi_2Te_3 at a growth temperature between 562 and 586 °C. Therefore, Bi-rich particles do not play a role in the growth of Bi_2Te_3 nanostructures presented here.

Note that we also observed Bi-rich Bi_2Te clusters on TiO_2 nanoparticles, as shown in Figure 1c, using EDX. This phase requires a Bi-rich melt and a temperature lower than 420 °C. They probably form during cool-down of the furnace. The TiO_2 nanoparticles are embedded in the incoming material, therefore indicating a catalytic function during the nucleation phase. These clusters have not led to the formation of nanostructures and are found on substrates that also contain a variety of Bi_2Te_3 nanostructures. This behavior is similar to the formation of Bi_2Te_2Se islands that were identified as a product of catalytic interaction with Au nanoparticles.[28]

TiO_2 catalyst particles were reported to increase belt yield and decrease the number of clusters in comparison with catalyst-free and Au-catalyzed growth.[25,31] Their role during the growth is less obvious than with Au nanoparticles since TiO_2 nanoparticles do not form large droplets at the tip of the belts during their catalytic activity. So, they either "aid" self-catalyzed growth and stay at the root of the belts or move forward with the tip without accumulating spherical precursor droplets. In particular, the tips of the two belts in an initial growth stage,

DOI: 10.1021/acs.cgd.6b01147
Cryst. Growth Des. 2016, 16, 6961−6966

pictured in Figure 1d, are free of any spherical clusters. Note, however, that VLS-type belts with amorphous catalytic tips have been reported in the literature.[17,30] The thickness of our belts is on the order of tens of nanometers since they are transparent to the electron beam. The root, on the other hand, is usually formed by a Bi_2Te_3 plate that is small compared to the size of the belt and visible in top-view images of the as-grown samples.

As the belts grow in general from clusters and platelets at an angle to the substrate, it can be concluded that the surface energy between the substrate and a liquid Bi_2Te_3 droplet, γ_{LS}(Si/droplet), must be larger than the surface energy between the droplet and the gaseous vapor phase, γ_{GS}(droplet/vapor), i.e., γ_{LS}(Si/droplet) > γ_{GS}(droplet/vapor). Evidence from Bi_2Te clusters suggests that TiO_2 plays a role in the initial phase of the nanostructure growth, but beyond that, the belts grow in a self-catalyzed process. Clusters and small plates are found at the root of belts in most cases, as shown in Figure 1e.

Effect of the Crystal Structure on the Belt Shape. Multidimensional Ehrlich–Schwöbel barriers are important to consider for understanding the belt growth described below. When adsorbates diffuse over the surface of the belt, edges present an energy barrier since the number of nearest neighbors at the edge is reduced. Therefore, the transition across an Ehrlich–Schwöbel barrier reduces the kinetic energy of the adsorbate. The space behind an Ehrlich–Schwöbel barrier is effectively a sink for adsorbates as they are more likely to settle once they are beyond the barrier. In this sense, an Ehrlich–Schwöbel barrier can also be seen as a reflective wall that contains adsorbates between boundaries. There are three types of edges, depending on their dimension, namely, kinks (one-dimensional), steps (two-dimensional), and terraces (three-dimensional), as illustrated in Figure 2.[34]

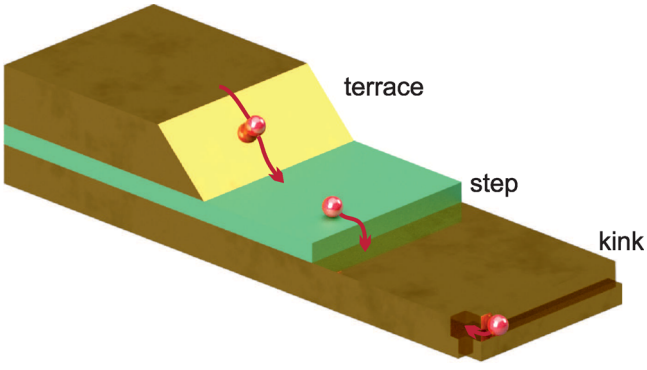

Figure 2. Ehrlich–Schwöbel barrier in one, two, and three dimensions. A two-dimensional Ehrlich–Schwöbel barrier (step) can be up to four atomic layers in height.

The shape of the tip of Bi_2Te_3 belts reflects the hexagonal crystal structure in the plane. Two growth directions, along the [210] and [110] directions, are commonly observed. The [110] direction is energetically more favorable and therefore dominating.[35] The [210] growth direction is depicted in Figure 3a, and the tip shape observed in Figure 1e is mapped onto the in-plane hexagonal coordinate system. The ratio between the (100) and (110) face fraction varies from belt to belt, whereby the complete absence of one of the faces was observed as well. A typical ratio is shown in the figure. The Bi and Te atoms appear ordered in a rectangular fashion along the projection in the [210] direction. The varying fraction of the two growth

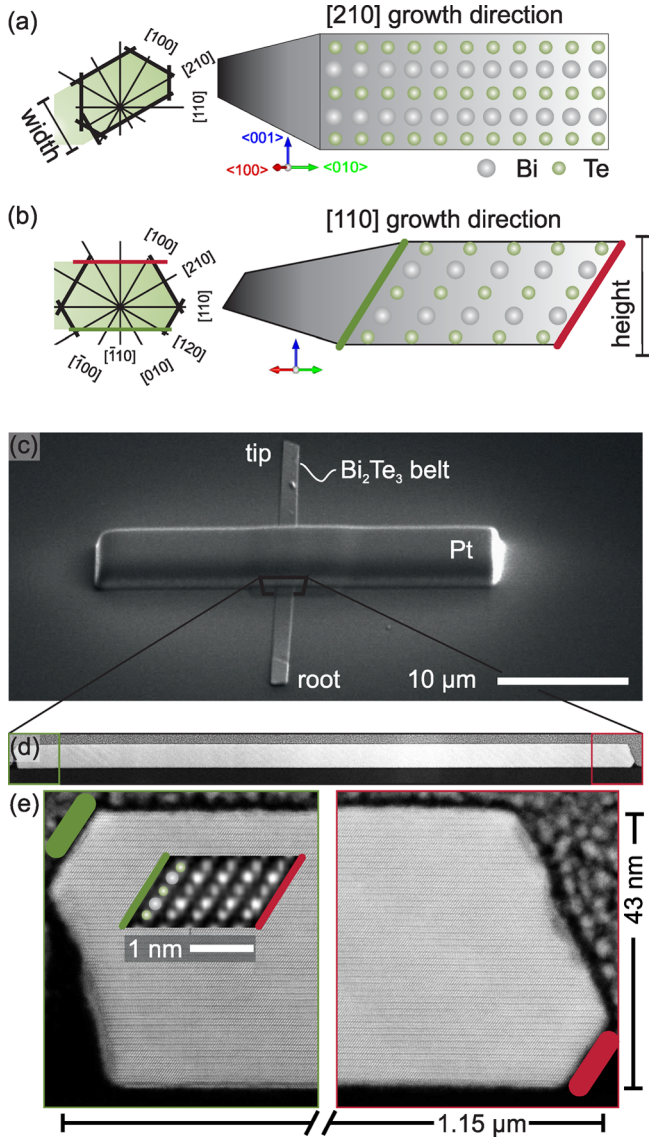

Figure 3. (a) Belt (green) growing along the [210] direction with in-plane hexagonal coordinate system superimposed on the tip. The (100) and (110) planes frame the tip. The projection down the [210] direction shows the rectangular arrangement of Bi (gray circles) and Te (green circles) atoms on the right. (b) Belt growing along the [110] direction. The (210) and (120) plane frame the tip. The projection down the [110] direction shows a slanted arrangement of Bi (gray) and Te (green) atoms on the right. (c) SEM micrograph of a Bi_2Te_3 belt prepared for FIB machining with a Pt protection layer. A lamella is extracted from the region indicated by the rectangle. (d) Low-magnification STEM micrograph of the cross-section of the belt. (e) Edges of the belt in cross-section. Lines (green and red) indicate faces that are parallel to atomic columns, as shown in the inset. The QLs (bright), separated by the van der Waals gap (dark), are clearly visible.

front faces could be the result of a dynamic process aiming at lowering the energy by moving the tip position. Also, it is energetically favorable to avoid sharp tips since they offer less binding sites for adsorbates. This, however, also depends on the material. Sn, e.g., forms rather flat tips in nanobelts, but GaN nanobelts are terminated by sharp tips.[2,36] The growth along the [110]-direction is depicted in Figure 3b. In this case, the tip is formed of (210) and (120) faces, which again have a ratio that varies from belt to belt. The projection along [110] reveals

DOI: 10.1021/acs.cgd.6b01147
Cryst. Growth Des. 2016, 16, 6961–6966

columns of Bi−Te units tilted by 30° to the surface normal of the belt.

The growth directions were confirmed analyzing the thin lamella extracted from the Bi_2Te_3 belt shown in Figure 3c. Moreover, looking at the cross-section of the belt allows us to connect the shape of the belt with its microstructure. The cross-section of the belt measures 1.15 μm in width and 43 nm in height, as shown in Figure 3, panels d and e, respectively. The tip is dominated by the (120) face and has therefore a triangular shape. The sidewalls are partly aligned with the faces that are to be expected for [110]-oriented structures, however, tilted by 30° with respect to the surface normal, as shown in Figure 3e. Interestingly, the shape is not perfectly rhombohedral, as expected from Figure 3b, but more compact, similar to the outline of SnO_2 nanoribbons, which could be a result of the growth mechanism discussed in the following.[37]

Step-Flow Growth Mode for Overgrowth. Larger Bi_2Te_3 belts consist of multiple layer stacks. The primary layer is the longest layer which forms the tip, as shown in Figure 4a. Secondary and tertiary layers grow on top, matching the width of the primary layer exactly; i.e., they do not extend beyond the boundaries of the primary later. The reason for the difference in length could be the reduced supply of precursor material coming from the substrate due to the crossing of two-dimensional Ehrlich−Schwöbel barriers on their way toward the tips. Thus, only adsorbates with the largest kinetic energy reach the tip, thereby slowing down the growth rate of the primary layer compared to the tertiary and secondary layer, thereby increasing the belt's height or thickness. The layer-by-layer growth mode is known in the context of thin film growth as Frank-van-der-Merwe growth.[38]

Most belts grow straight as quasi-one-dimensional crystals, as shown in Figure 4b. In the following, we will discuss two examples that are different and quite unique in terms of size and intriguing growth features. The first one is a branched belt. The branching point is located near the base, forming an angle of 60° with the direction of the main belt, as shown in Figure 4c. This corresponds to the [100] or [010] direction (which are indistinguishable), if the growth direction of the belt is [110].

The branch only measures half of the length of the main belt, despite the fact that the growth rates for both crystal directions should be identical. Here, the reason for the reduced growth rate of the branch is a cluster at its very tip, as shown in Figure 4d. Right at the base of the cluster, the width of the belt is strictly limited by the width of the cluster. In-plane growth perpendicular to the growth direction on both sidewalls of the belt has led to a rough tapering similar to BiTe belts grown by Hsin et al.[39] The sidewalls extrude on multiple locations at the same time, leading to the formation of indented triangles that gradually fill up at intersection points of two extrusions. These triangles are characteristic for broadening of belts. In fact, the branch itself is an extreme example of broadening, as indicated by a green line in Figure 4e, mapping to the edge of a triangle, i.e., the edge of an extension of the sidewall (bottom-side of the main part). Several layers extend from the branch intersection. Adsorbates attach to corners at the growth front so that the layers extend in a very compact growth front, as shown in Figure 4f.

Figure 4g shows triangles and steps with varying heights between 50 and 300 nm. Steps are slanted and smoothen the three-dimensional Ehrlich−Schwöbel barrier. The initial height of the primary layer can be estimated from the distance between the position of a triangle and the lower position of the

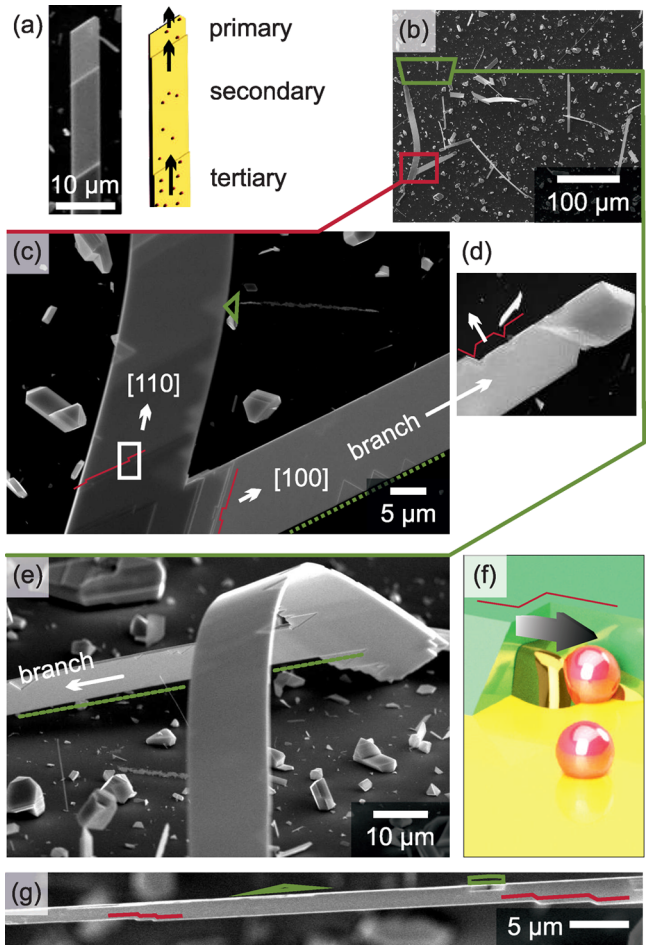

Figure 4. (a) SEM image of the tip of a Bi_2Te_3 belt. Three layers, labeled primary, secondary, and tertiary layer, can be distinguished as gradually darker terraces. Adsorbate density decreases from tertiary to primary layer (metallic spheres). (b) As-grown sample with several belts and many clusters. The red rectangle indicates the branched belt in (c). The green rectangle indicates the side-view in (e). (c) Top view of the branching point. The angle between the branch and the main part is 60° (measured angle smaller due to tilt of the belt). Step edges with dips from step-flow growth (red lines), one of several triangles (green), and the sidewall of the branch (green line) are indicated. A white rectangle indicates the location of the process shown in (f). (d) The tip of the branch is formed by a cluster. The sidewall of the topmost layer is roughly tapered (red line). (e) View from underneath. The branch is an extension of one of the growth fronts toward the sidewalls (green line maps to green line in (c)). (f) Schematic drawing of the growth process. The secondary layer (green) grows on top of the primary layer (yellow) by migration of adatoms to an edge in the growth front indicated by an amorphous cluster (yellow) that moves parallel to the terrace step edge. (g) Side-view of a belt showing step edges (red) and triangular indentations (green) resulting from step-flow and broadening. Note that the triangular indentations appear as rectangles in side view.

primary layer to be ∼300 nm, which agrees with a tripling of the thickness through layer-by-layer growth.

Step-Flow Growth against the Flow. The second unique example is a belt with a plate protruding perpendicular to its growth direction, as shown in Figure 5a. Precursor atoms adsorb onto the plate directly, i.e., not supplied by diffusion along the belt, since the layers on the plate grow against the diffusion direction (cf. Figure 5b). A droplet is found on the surface of the belt in Figure 5b, which could be an example of a

DOI: 10.1021/acs.cgd.6b01147
Cryst. Growth Des. 2016, 16, 6961−6966

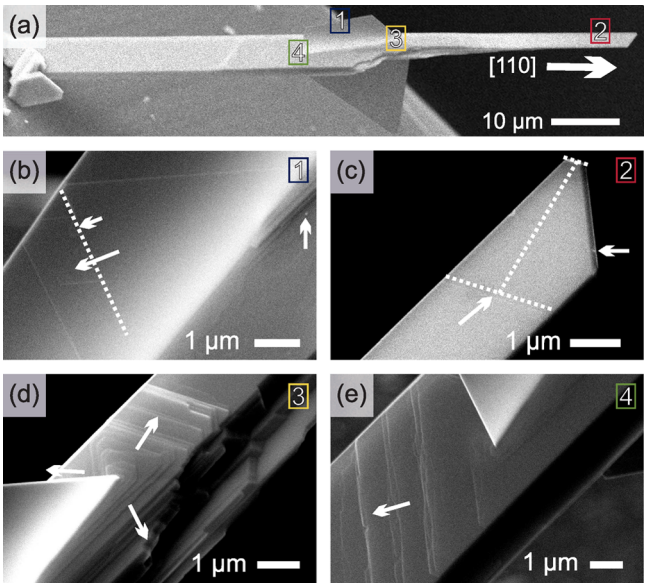

Figure 5. (a) Belt with a perpendicularly protruding plate (SEM micrograph). The growth direction is indicated by an arrow. Numbers indicate points of interest. (b) Layer-by-layer growth in triangular shapes (dotted line and white arrows) on top of the plate. The white arrow on the right indicates the formation of a droplet, which could act as a catalyst for the formation of protrusions. (c) The tip has two growth faces, as indicated. A spot on the wider growth front is indicated by a white arrow. The layer indicated by the dotted line grows with its growth front parallel to the narrower edge of the tip. (d) Toward the base of the plate additional layers grow in all directions, away from the intersection point (white arrows) and not only in one direction. (e) Toward the lower base of the plate wavy step-edges are observed, propagating toward the base of the belt.

catalytic particle that initiates growth and is responsible for protrusions. The tip of the belt is thinner than the bottom part, consistent with growth of additional layers at the bottom. A secondary layer grows with a growth front at an angle of 60° to the main face of the tip, as shown in Figure 5c. Thus, parallel alignment of primary and secondary layers, as seen in Figure 4a, is not necessarily the case which is another evidence for alternating growth fronts assuming that the starting orientation is the same for all layers. A coarse spot of the size of the droplet in Figure 5b is located at the tip. This could be a catalytic particle responsible for growth at the tip similar to the growth mode of the layers on top, as it is pictured schematically also in Figure 4c (circle).

The sidewalls of the belt are strongly disrupted near the upper intersection of the plate with the belt. First, the width of the belt halves compared to the width at the lower end. Second, layers of various length and width extrude from the sidewalls. Third, the step-flow growth observed above is replaced by an island-type growth mode, fueled by material supplied from the edge of the plate. This is analogous to high flow growth experiments with Bi_2Te_3 that yield many small platelets instead of a few long belts.

The situation is completely different at the other end of the intersection, i.e., between the plate and the belt, as shown in Figure 5e. Layers on the belt grow in step-flow growth toward the base. A wavy terrace edge is characteristic of "growth against the flow", i.e., a higher adatom flow from the lower steps than from the higher steps.[40]

CONCLUSIONS

In Bi_2Te_3 belts, layers grow in a step-flow mode, starting from the root of the structure. Several layers can form simultaneously. The terrace edges are slanted and either parallel or rotated by 120° with respect to the tip, apparently alternating between the two orientations. The growth direction of the belts is ⟨110⟩. Their width increases through broadening—a mechanism that leads to extrusions and triangular defects on the flat surfaces of the structures. TiO_2 catalyst particles play the role of a nucleation center for the adsorbates on the Si substrate. The catalyst may be present at the tip as well, potentially leading to tip-catalyzed growth, although evidence in the form of spherical clusters were observed.

The demonstration of step-flow growth of Bi_2Te_3 nanobelts is an important finding since epitaxial growth is a key ingredient for the production of device materials. This growth mode has not been realized in MBE growth of Bi_2Te_3 thin films, which are dominated by the merging of growth "islands". Compared to MBE growth, vapor transport growth occurs at atmospheric pressure and for substrate temperatures twice as high as for MBE growth. The single-crystalline nature of the belts makes them potentially better suited for transport experiments and interesting candidates for the growth of heterostructure devices.

AUTHOR INFORMATION

Corresponding Author

*E-mail: Thorsten.Hesjedal@physics.ox.ac.uk. Phone: +44 (0) 1865 272235. Fax: +44 (0)1865 274000.

Notes

The authors declare no competing financial interest.

ACKNOWLEDGMENTS

This publication arises from research funded by the John Fell Oxford University Press (OUP) Research Fund and funding from the European Union Seventh Framework Programme under Grant Agreement 312483-ESTEEM2 (Integrated Infrastructure Initiative I3) and transnational access to MPI-FKF (WP13). P.S. acknowledges partial funding from EPSRC, Corpus Christi College (Oxford), and the Studienstiftung des deutschen Volkes (Germany). A.A.H. acknowledges the support through the EPSRC Platform Grant (Grant No. EP/M020517/1). RCaH is acknowledged for their hospitality. Ulrike Eigenthaler (MPI-IS) is acknowledged for preparing the FIB samples.

REFERENCES

(1) Pan, Z. W.; Dai, Z. R.; Wang, Z. L. *Science* **2001**, *291*, 1947−1949.
(2) Bae, S. Y.; Seo, H. W.; Park, J.; Yang, H.; Park, J. C.; Lee, S. Y. *Appl. Phys. Lett.* **2002**, *81*, 126−128.
(3) Zhu, Y.-C.; Bando, Y.; Xue, D.-F. *Appl. Phys. Lett.* **2003**, *82*, 1769−1771.
(4) Xie, T.; Lin, Y.; Wu, G.; Yuan, X.; Jiang, Z.; Ye, C.; Meng, G.; Zhang, L. *Inorg. Chem. Commun.* **2004**, *7*, 545−547.
(5) Liu, H.; Cui, H.; Han, F.; Li, X.; Wang, J.; Boughton, R. I. *Cryst. Growth Des.* **2005**, *5*, 1711−1714.
(6) Shi, W.; Yu, J.; Wang, H.; Zhang, H. *J. Am. Chem. Soc.* **2006**, *128*, 16490−16491.
(7) Yan, Y.; Liao, Z.-M.; Zhou, Y.-B.; Wu, H.-C.; Bie, Y.-Q.; Chen, J.-J.; Meng, J.; Wu, X.-S.; Yu, D.-P. *Sci. Rep.* **2013**, *3*, 1264.
(8) Comini, E.; Faglia, G.; Sberveglieri, G.; Pan, Z.; Wang, Z. L. *Appl. Phys. Lett.* **2002**, *81*, 1869.
(9) Kane, C. L.; Mele, E. J. *Phys. Rev. Lett.* **2005**, *95*, 146802.

DOI: 10.1021/acs.cgd.6b01147
Cryst. Growth Des. 2016, 16, 6961−6966

(10) Bernevig, B. A.; Hughes, T. L.; Zhang, S.-C. *Science* **2006**, *314*, 1757−1761.
(11) Nolas, G. S.; Sharp, J.; Goldsmid, H. J. In *Thermoelectrics*; Hull, R., Osgood, R. M., Sakaki, H., Zunger, A., Eds.; Springer Series in Materials Science; Springer: Berlin, Heidelberg, 2001; Vol. *45*.
(12) Xiu, F.; He, L.; Wang, Y.; Cheng, L.; Chang, L.-T.; Lang, M.; Huang, G.; Kou, X.; Zhou, Y.; Jiang, X.; Chen, Z.; Zou, J.; Shailos, A.; Wang, K. L. *Nat. Nanotechnol.* **2011**, *6*, 216−221.
(13) Ando, Y. *J. Phys. Soc. Jpn.* **2013**, *82*, 102001.
(14) Peng, H.; Dang, W.; Cao, J.; Chen, Y.; Wu, D.; Zheng, W.; Li, H.; Shen, Z.-X.; Liu, Z. *Nat. Chem.* **2012**, *4*, 281−286.
(15) Guo, Y.; Lin, L.; Zhao, S.; Deng, B.; Chen, H.; Ma, B.; Wu, J.; Yin, J.; Liu, Z.; Peng, H. *Adv. Mater.* **2015**, *27*, 4315−4321.
(16) Zheng, W.; et al. *Nat. Commun.* **2015**, *6*, 6972.
(17) Zou, Y.; Chen, Z. G.; Huang, Y.; Drennan, J.; Zou, J. Au-catalyzed and catalyst-free growth of one-dimensional Bi_2Se_3 nanostructures. 2014 Conference on Optoelectronic and Microelectronic Materials Devices, 2014; pp 11−14.
(18) Zhang, Y.; Chang, C.-Z.; He, K.; Wang, L.-L.; Chen, X.; Jia, J.-F.; Ma, X.-C.; Xue, Q.-K. *Appl. Phys. Lett.* **2010**, *97*, 194102.
(19) Harrison, S. E.; Li, S.; Huo, Y.; Zhou, B.; Chen, Y. L.; Harris, J. S. *Appl. Phys. Lett.* **2013**, *102*, 171906.
(20) Kampmeier, J.; Borisova, S.; Plucinski, L.; Luysberg, M.; Mussler, G.; Grützmacher, D. *Cryst. Growth Des.* **2015**, *15*, 390−394.
(21) Liu, Y.; Li, Y. Y.; Rajput, S.; Gilks, D.; Lari, L.; Galindo, P. L.; Weinert, M.; Lazarov, V. K.; Li, L. *Nat. Phys.* **2014**, *10*, 294−299.
(22) Hong, S. S.; Cha, J. J.; Kong, D.; Cui, Y. *Nat. Commun.* **2012**, *3*, 757.
(23) Jauregui, L. A.; Pettes, M. T.; Rokhinson, L. P.; Shi, L.; Chen, Y. P. *Sci. Rep.* **2015**, *5*, 8452.
(24) Park, Y.-S.; Lee, J. S. *J. Nanopart. Res.* **2014**, *16*, 2226.
(25) Schönherr, P.; Zhang, F.; Kojda, D.; Mitdank, R.; Fischer, S.; Hesjedal, T.; Albrecht, M. *Nanoscale Res. Lett.* **2016**, *11*, 308.
(26) Cha, J. J.; Williams, J. R.; Kong, D.; Meister, S.; Peng, H.; Bestwick, A. J.; Gallagher, P.; Goldhaber-Gordon, D.; Cui, Y. *Nano Lett.* **2010**, *10*, 1076−1081.
(27) Alegria, L. D.; Schroer, M. D.; Chatterjee, A.; Poirier, G. R.; Pretko, M.; Patel, S. K.; Petta, J. R. *Nano Lett.* **2012**, *12*, 4711−4714.
(28) Schönherr, P.; Collins-McIntyre, L. J.; Zhang, S.; Kusch, P.; Reich, S.; Giles, T.; Daisenberger, D.; Prabhakaran, D.; Hesjedal, T. *Nanoscale Res. Lett.* **2014**, *9*, 127.
(29) Lee, J. S.; Brittman, S.; Yu, D.; Park, H. *J. Am. Chem. Soc.* **2008**, *130*, 6252−6258.
(30) Kong, D.; Randel, J. C.; Peng, H.; Cha, J. J.; Meister, S.; Lai, K.; Chen, Y.; Shen, Z.-X.; Manoharan, H. C.; Cui, Y. *Nano Lett.* **2010**, *10*, 329−333.
(31) Schönherr, P.; Prabhakaran, D.; Jones, W.; Dimitratos, N.; Bowker, M.; Hesjedal, T. *Appl. Phys. Lett.* **2014**, *104*, 253103.
(32) Predel, B. *Bi-Te (Bismuth-Tellurium)*; Landolt-Börnstein - Group IV Physical Chemistry 5b; 1992; pp 1−7.
(33) Ferhat, M.; Tedenac, J. C.; Nagao, J. *J. Cryst. Growth* **2000**, *218*, 250−258.
(34) Lagally, M. G.; Zhang, Z. *Nature (London, U. K.)* **2002**, *417*, 907−910.
(35) Lv, H. Y.; Liu, H. J.; Shi, J.; Tang, X. F.; Uher, C. *J. Mater. Chem. A* **2013**, *1*, 6831−6838.
(36) Zhang, J.; Yang, Y.; Jiang, F.; Xu, B.; Li, J.; Wang, X.; Wang, S. *Nanotechnology* **2005**, *16*, 2887.
(37) He, R.; Law, M.; Fan, R.; Kim, F.; Yang, P. *Nano Lett.* **2002**, *2*, 1109−1112.
(38) Woodruff, D. P. *Philos. Trans. R. Soc., A* **2015**, *373*, 20140230.
(39) Hsin, C.-L.; Wingert, M.; Huang, C.-W.; Guo, H.; Shih, T.-J.; Suh, J.; Wang, K.; Wu, J.; Wu, W.-W.; Chen, R. *Nanoscale* **2013**, *5*, 4669.
(40) Bales, G. S.; Zangwill, A. *Phys. Rev. B: Condens. Matter Mater. Phys.* **1990**, *41*, 5500−5508.

DOI: 10.1021/acs.cgd.6b01147
Cryst. Growth Des. 2016, 16, 6961−6966